

Design of a 10 MW/m²-heat-flux removal system for a W7-X divertor tile using triply periodic minimal surfaces

Original

Design of a 10 MW/m²-heat-flux removal system for a W7-X divertor tile using triply periodic minimal surfaces / Quamori Tanzi, A.; Cammi, A.; Marocco, L.; Savoldi, L.. - In: CASE STUDIES IN THERMAL ENGINEERING. - ISSN 2214-157X. - 63:(2024). [10.1016/j.csite.2024.105405]

Availability:

This version is available at: 11583/2994907 since: 2024-11-30T17:18:36Z

Publisher:

ELSEVIER

Published

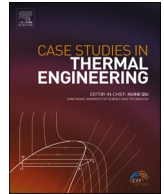
DOI:10.1016/j.csite.2024.105405

Terms of use:

This article is made available under terms and conditions as specified in the corresponding bibliographic description in the repository

Publisher copyright

(Article begins on next page)



Design of a 10 MW/m²-heat-flux removal system for a W7-X divertor tile using triply periodic minimal surfaces

Alessio Quamori Tanzi^a, Antonio Cammi^b, Luca Marocco^b, Laura Savoldi^{a,*}

^a MAHTEP Group, Dipartimento Energia "Galileo Ferraris", Politecnico di Torino, Italy

^b MAHTEP Group, Department of Energy, Politecnico di Milano, Milan, Italy

ARTICLE INFO

Keywords:

Divertor
TPMS
Gyroid
Diamond

ABSTRACT

In nuclear fusion reactors, the heat removal from high-heat-flux components such as the divertor has always been a challenge as the heat flux is anticipated to easily overcome 10 MW/m², as it is the case for the divertor tiles in the W7-X stellarator. In this paper a new cooling solution, relying on a Triply Periodic Minimal Surface lattice, is proposed and investigated. The analysis first focuses on the identification of the optimal lattice with a dedicated investigation on a reduced computational domain. The analysis with the best candidate is moved to a 30 cm × 10 cm divertor tile, to prove the compliance with the operating constraints. The tile with the gyroid lattice with unit cell size of 10 × 10 × 5 mm³ is shown to be capable to withstand a heat flux of 10 MW/m², distributed over a heated length of 10 cm, when 1.25 kg/s of subcooled water are used for cooling, resulting in a pressure drop <0.6 MPa and tolerating a very limited fluid boiling just around the inlet/outlet manifolds. Eventually, the benefits of this configuration, when compared to others, in terms of enhancement of the performance and structure lightning, are discussed.

1. Introduction

In the context of magnetic-confinement nuclear fusion devices, one of the unresolved engineering challenges is the removal of the huge heat flux impacting components such as the divertor. Divertor tiles/plates/targets in fact protect the vacuum vessel in the areas where the magnetic flux lines are open, leading to heat and particle exhaust from the fusion plasma. Entire experimental facilities, including the Italian Divertor Tokamak Test facility [1] are being constructed to find viable solutions for the open issue of the removal of the enormous amount of heat released in that component. In the W7-X, the largest stellarator worldwide [2], for instance, the divertor tiles for the next test campaign [3] should be designed to remove safely up to 10 MW/m² in normal operating conditions, and up to 15 MW/m² in the case of off-normal conditions. Similar values are expected in ITER, the tokamak experimental reactor under construction in France [4], while slow transients up to 20 MW/m² are foreseen in the next generation reactors aiming at producing electricity [5].

To ensure compatibility with tritium, divertor tiles (or targets) in W7-X typically feature a tungsten layer (or armor), as tungsten has the highest melting point among metals. This tungsten layer, 1-mm thick to minimize the divertor weight,¹ is joined to the cooling structure, which is usually embedded in a block of a copper-based alloy (CuCrZr in the of W7-X [3]), via a 1-mm soft copper interlayer.

* Corresponding author.

E-mail address: laura.savoldi@polito.it (L. Savoldi).

¹ Note that, based on expected erosion rates in W7-X, a minimum thickness of 0.2 mm for a cumulative exposure time of ~300 h during the lifetime of W7-X is estimated in Ref. [7].

The cooling channels for the coolant (subcooled water) are indeed located within the CuCrZr bulky block, and typically features turbulence promoters such as twisted tapes [3] to increase the heat removal. Recently, different cooling configurations such as sub-millimeter microchannels, manufacturable with Additive Manufacturing (AM) techniques, are becoming credible based on thermal-hydraulic and thermo-mechanic analyses [6].

As an alternative to micro-channels or other cooling innovative cooling structures [6–8] this study considers as potential effective heat sinks for divertor tiles another family of cooling structures made possible by AM, and namely Triply Periodic Minimal Surfaces (TPMS), based on promising preliminary results shown in Ref. [9]. Although a previous successful attempt to design a heat sink with these structures was performed on a mirror of the Electron Cyclotron Resonance Heating transmission line for the DTT facility [10] this is the first time TPMS lattices are being used as heat sinks within in-vessel high heat flux components of a fusion reactor.

TPMS are periodic surfaces with zero mean curvature and free of self-intersections, obtained from the combination of trigonometric (sine and cosine) functions in the three spatial directions. They allow the realization of highly interconnected lattices, capable to provide a significant enhancement of the heat transfer to the operating fluid due to the increase in the heat transfer surface and the particular flow structure imparted to the fluid. Among the different possible TPMS, the suitability of Gyroid (G) and Diamond (D) lattices as heat sinks has been already shown by several authors ([11–14]). The consensus about which of the two is the most efficient cooling structure is not unanimous, also in view of the different lattice layouts, structures and flow regimes investigated by the different authors. A better performance of the D, compared to G, is computed in Ref. [14] for a heat sink with an ideal porosity of 100 % (i.e., where the different fluid regions are separated by a surface with zero thickness). On the contrary, in Ref. [13] the G lattice is shown through a numerical study to have a better overall performance, combining both heat transfer and pressure drop, than the D one, at least at low Reynold number ($Re < 50$) and with a lattice porosity of $\sim 45\%$. A detailed numerical investigation in Ref. [15] allows verifying that, at low Re, the D lattice pays the enhanced heat transfer with a much larger pressure drop than the G one. The investigation on a counter-current heat exchanger conducted in Ref. [11] shows how the supremacy of the D structure over the G one depends on the range of Re, and the latter is computed to have a better performance at $Re > 15000$. Note, however, that part of the above-mentioned results are obtained comparing different varieties of G and D structures, often referring to “solid”, and not only “sheet” lattices.

Since the choice among the two topologies seems to be strongly affected by the specific operating conditions and lattice geometrical features, both the D and G topologies have been considered as potential candidates for heat sinks in the divertor tile in this study. The tile considered here has a toroidal width of 10 cm and a poloidal extension of 30 cm, closely matching the dimension of those described in Ref. [8] and featuring the layered structure shown in Fig. 1a. The coolant, subcooled water at 30 °C, flows in and out through dedicated ducts on the backside of the tile, as depicted in Fig. 1a. The tile poloidal length considered here (30 cm) reduces the need for hydraulic connections on the back of the tiles, as opposed to the standard 10 cm \times 10 cm square tiles [6], as the tile-to-tile connections increase the complexity of the device, as well as the coolant pressure drop. The heat flux value of 10 MW/m² [7] in steady state [3] over a maximum poloidal length of 10 cm is taken as the design value. The heat should be removed from the tile while ensuring that the coolant remains in a single phase as much as possible, to avoid the risk of approaching the Critical Heat Flux (CHF) region and thus of film boiling. Following a common engineering approach to meet this constraint, the tile cooling structure should be designed so that the temperature at the solid-fluid interface does not exceed the saturation temperature, evaluated conservatively at the outlet pressure.

To reduce investment, modifications of the water supply outside the machine should be avoided [3], so that the current water-cooling infrastructure should be utilized, offering 12 supply lines, each with a flow rate of 5 kg/s (one pump) and an acceptable pressure drop of 15 bar [7]. As a result, the new target surface is expected to be divided into 12 target modules, with each module connected to a single supply line. The maximum mass flow rate available for a 60 cm \times 40 cm divertor module is equal to 5 kg/s, and the maximum inlet pressure can reach 2.5 MPa with a pressure drop of 1.5 MPa along the module. However, as shown in Fig. 1b, when a parallel network of micro-channels is deployed [8], the hydraulic impedance is such to require in perspective two cooling loops per module, each with a flow rate of 5 kg/s (two pumps). This setup would increase the overall cost of the installation. According to the micro-channels design, in each loop four tiles were connected in parallel due to the high pressure drop in the microchannel configuration, which precluded the use of a single loop for the module. In contrast, this study aims at a single cooling loop for the entire divertor module, as illustrated in Fig. 1c. This approach leverages the existing supply line, substantially reducing costs by eliminating the need for an additional pump.

The cooling effectiveness of the different lattice topologies is assessed by determining the maximum heat flux they can handle while maintaining the fluid in a single phase (solid-fluid interface temperature everywhere below the saturation temperature at 1 MPa, i.e. $\sim 180^\circ\text{C}$) and keeping the pressure drop along the entire tile below 0.75 MPa. Additional constraints, which can be verified a posteriori, include keeping the maximum temperature of the CuCrZr below its softening point, and the tungsten hot-spot temperature below 1200 °C.

Since an infinite number of possible D and G configurations can be generated by analytical functions, a methodology is first identified and presented for selecting the most suitable TPMS layout. This methodology involves a numerical simulation campaign conducted on a reduced computational domain (sketched in Fig. 1a), where several parametric analyses investigate not only the lattice porosity, as commonly done in other studies, but also, innovatively, the rotation of the lattice with respect to the main flow direction and the displacement of the lattices relative to the heated surface. The optimal TPMS configuration identified through this process is then implemented as the cooling structure for the actual divertor tile geometry, ensuring the expected performance in terms of maximum sustainable heat flux and pressure drop are achieved. A comparison with the expected performance of the configuration equipped with micro-channels is also provided.

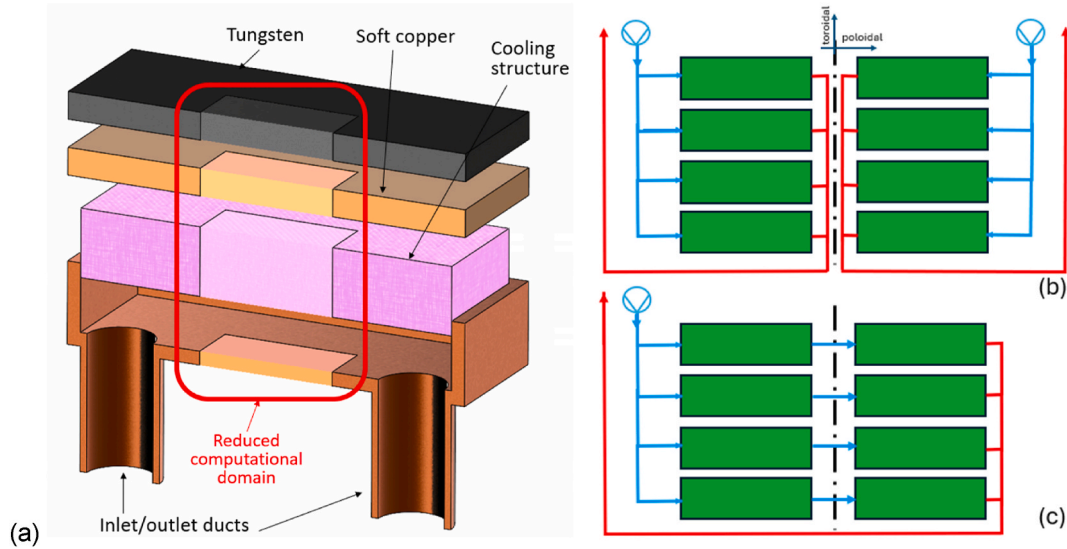


Fig. 1. – Sketch of the layered structure of a tile for the W7-X divertor considered in the present study. From top to bottom: 1-mm layer of tungsten, 1-mm layer of soft copper, the CuCrZr layer where the cooling structure is located, with inlet and outlet ducts (not to scale) (a). Schematic of the cooling loop of the divertor tiles in a module of the W7-X divertor, with 30 cm × 10 cm tiles connected hydraulically in parallel using two loops (b) or a single loop (c).

2. Methodology

The cooling performance of a subsection of the tile, shown in the inset of Fig. 1a, is analyzed numerically. This reduced computational domain covers a small part of the entire multi-layer structure, specifically 2 lattice unit cells in the main flow (poloidal) direction. This choice seems a reasonable compromise between the different needs of having a computational domain of a limited extension, to limit the computational effort, and of having a number of lattice cells capable to capture representative flow conditions, considering that the development region extends over a non-negligible part of the domain.

It is then assumed that the thermal-hydraulic assessment on this reduced domain represents the lattice performance when implemented in the divertor tile under consideration, given that the flow is expected to be evenly distributed across the lattice, in the direction perpendicular to the flow. Except for small portions of the manifold regions, this assumption is successfully verified a posteriori, as the simulations on the reduced computational domain turn out to give representative results with respect to the full tile.

The constraints on pressure drop and mass flow rate are scaled to the length of the reduced computational domain, while the constraints on saturation temperature and maximum CuCrZr temperature remain unchanged.

2.1. Lattice selection for the reduced computational domain

The software Ntop [16] has been utilized to generate the geometry of the reduced computational domain, including the **D** and **G** lattices, and a cartesian set of coordinates (x, y, z) has been adopted for the lattice generation. Note that TPMS-based structures can be generated by means of an iso-surface, defined by a level-set function $f(x, y, z) = 0$, which splits the volume into two regions. If one region contains solid material and the other contains fluid, the resulting lattice is classified as "solid". Alternatively, if the iso-surface is extruded by a given quantity $2c$ in the normal direction ($f(x, y, z) = \pm c$), it creates a third volume that completely separates the two complementary regions. Typically the region included within the two iso-surfaces constitutes a solid wall separating two fluid regions. The resulting lattice, which is the only one considered in this paper, is called "sheet". Note that "sheet" structure is reported in literature to have better performance in heat transfer than the corresponding "solid" structure [12].

Each couple of fluid regions generated by the selected topologies are identical, so that the two fluid channels split equally the total coolant mass flow rate. This is not the case for other more complex (and possibly efficient [17]) lattices, such as the SplitP, for instance, where the fluid regions of the "sheet" configurations are not identical, resulting in uneven split of the fluid flow rate and possibly uneven cooling effectiveness.

Different alternative layouts of the **D** and **G** lattices have been investigated in the reduced computational domain, to identify the best compromise between thermal and hydraulic performances, under the constraints of keeping the coolant below the saturation point.

Given a unit lattice cell size, the lattices for all different topologies can be generated adjusting different parameters. The most common one is the porosity, which, in the case of the "sheet" configurations is controlled by the amplitude of the extrusion of the iso-surface, affecting the wall thickness. When the lattice is used as a heat sink in a channel with a main flow direction s , as in the case at hand, another key parameter is the angle between the lattice principal axes and the flow direction. The principal directions along

which the lattice is generated determine the dominant flow directions, as shown in Fig. 2a and b for the **D** and in Fig. 2c and d for the **G** lattices, respectively. In Fig. 2a, where the lattice is generated with one of the principal axis parallel to the main flow direction, the fluid moves into channels that have an angle of $\frac{\pi}{4}$ with respect to s . If the x -axis of the lattice is rotated by an angle of $\frac{\pi}{4}$ with respect to s (Fig. 2b), the main flow direction coincides with s . The **D** lattice considered here is then generated according to Fig. 2b. In the case of the **G** lattice, no rotation is needed as one of the dominant flow directions is already aligned with the principal flow direction.

In addition to porosity and lattice rotation, a third important parameter is the displacement d of the lattice with respect to the heated surface. This displacement is achieved by a rigid translation of the lattice in the plane perpendicular to the flow direction s , on which the direction of the heat flux lies. Fig. 3 illustrates how a suitable displacement of both **D** and **G** lattices can create straight (“clear”) channels for the fluid, aligned with the s direction, just underneath the heated surface. The lattice with no displacement is labelled “Normal” (\mathbb{N}), while the displaced one is labelled “Channels” (\mathbb{C}).

The unit lattice cell size has been set equal to 10 mm along the s direction, and 10 mm or 5 mm in the direction perpendicular to s . In the latter case, the lattice cells experience a sort of stretching in the direction of the flow, that should help in reducing the pressure drop, as pointed out in Ref. [18]. The average thickness of the sheet structure is maintained above 0.8 mm to meet manufacturing constraints for the AM powder-and-laser technique [19].

As it is known from previous studies [9] that only the first lattice cell, underneath the heated surface strongly contributes to the heat removal, the total thickness of the cooling structure has been selected equal to the unit lattice cell, i.e. 10 mm or 5 mm, see Fig. 4. Three porosity values (reported in Table 1) have been tested, obtained with a wall thickness of the lattice of 0.8 mm, 1.0 mm and 1.2 mm, respectively, and two different displacement of the lattices have been investigated (“Normal”, \mathbb{N} , and Channels”, \mathbb{C} , respectively, as already shown in Fig. 3). It has already been shown, in fact, that the thermal performance of TPMS-based lattice is very sensitive to TPMS wall thickness and pore diameter [20]. For a gyroid lattice at small Re number, the heat removal capability was shown numerically to increase when the wall thickness was increased (and the pore size, as well as the porosity, reduced). Note, however, that apparently the contrary was found for a diamond lattice [21].

Based on this rationale, a total of 18 different configurations, listed in Table 1, were generated and analyzed as explained in Section 2.2. From Table 1 it is evident that, from the geometrical point of view, the \mathbb{N} and \mathbb{C} configurations share, for the same lattice topology, the same porosity (defined as the ratio between the fluid volume V_f and the total volume of the lattice V_{tot}) and the same surface-to-volume ratio (defined as the ratio of wetted surface A_w over V_f).

The **G** lattices have, for the same lattice cell size, a higher porosity than the corresponding **D** lattices, and a lower value of surface-to-volume ratio. These effects are consequence of the more packed structure in the **D** lattices. This could be explained looking at the level-set functions for the two lattices, and namely:

$$\sin\left(\frac{2\pi}{L_x}x\right)\cos\left(\frac{2\pi}{L_y}y\right) + \sin\left(\frac{2\pi}{L_y}y\right)\cos\left(\frac{2\pi}{L_z}z\right) + \sin\left(\frac{2\pi}{L_z}z\right)\cos\left(\frac{2\pi}{L_x}x\right) = 0 \quad (1)$$

for the **G** lattices, and

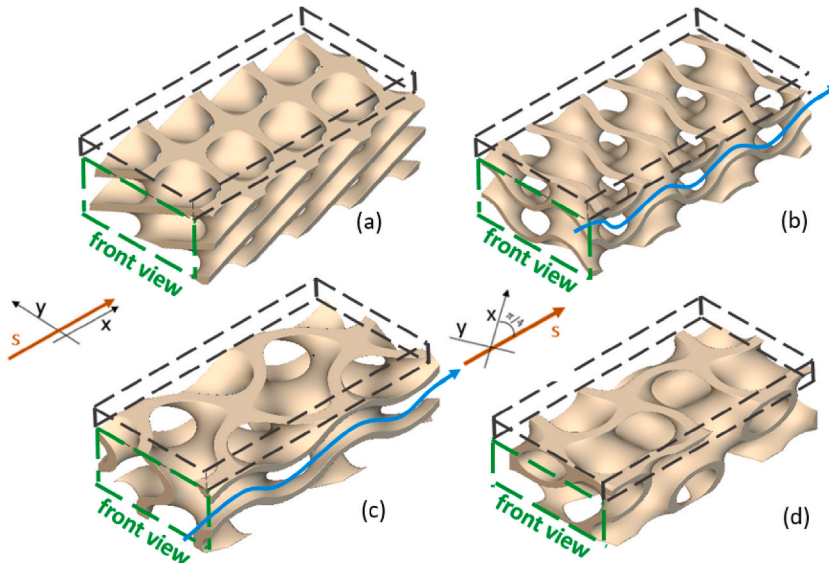


Fig. 2. Reduced computational domain where the cooling structures are **D** lattices (a, b) and **G** lattices (c,d) with the direction of the principal flow direction s aligned with the axis x along which the lattice is generated (a,c) or rotated by 45° with respect to the axis x in the plane (x,y) . The light-blue arrows remark the main flow direction. (For interpretation of the references to color in this figure legend, the reader is referred to the Web version of this article.)

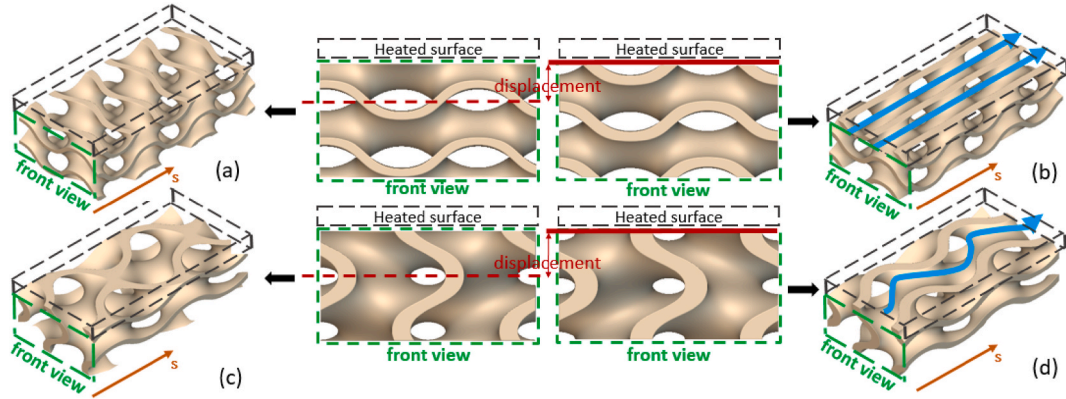


Fig. 3. – Reduced computational domain obtained using the **D** lattice in the **N** (a) and **C** (b) configurations, and the **G** lattice in the **N** (c) and **C** (d) configurations, respectively. The fluid channels underneath the heated surface in the **C** configurations are also shown with light-blue arrows in (b) and (d). (For interpretation of the references to color in this figure legend, the reader is referred to the Web version of this article.)

$$\sin\left(\frac{2\pi}{L_x}x\right)\sin\left(\frac{2\pi}{L_y}y\right)\sin\left(\frac{2\pi}{L_z}z\right) + \sin\left(\frac{2\pi}{L_x}x\right)\cos\left(\frac{2\pi}{L_y}y\right)\cos\left(\frac{2\pi}{L_z}z\right) + \cos\left(\frac{2\pi}{L_x}x\right)\sin\left(\frac{2\pi}{L_y}y\right)\cos\left(\frac{2\pi}{L_z}z\right) + \cos\left(\frac{2\pi}{L_x}x\right)\cos\left(\frac{2\pi}{L_y}y\right)\sin\left(\frac{2\pi}{L_z}z\right) = 0 \quad (2)$$

for the **D** lattices, being L_x , L_y and L_z the characteristic cell dimensions along x , y and z , respectively. According to the literature, the surface area values S for the two level set functions are 3.09 for the Gyroid lattice in Eq. (1) and 3.84 square units for the Diamond lattice in Eq. (2), within a unit cell box ($L_x = L_y = L_z = 1$), making the **D** lattice more compact than the **G** one.

The surface area S of an implicit surface defined by $f(x, y, z) = 0$ ($f = \mathbf{G}$ or **D**) can be calculated using the integral in Eq. (3)

$$S = \iint_{\Sigma} \frac{|\nabla f(x, y, z)|}{\left| \frac{\partial f}{\partial z} \right|} dA \quad (3)$$

where $\nabla f(x, y, z)$ is the gradient of the function $f(x, y, z)$, $|\nabla f(x, y, z)|$ is the magnitude of the gradient and $\frac{\partial f}{\partial z} = \nabla f(x, y, z) \cdot \mathbf{k}$ represents the derivative of function f with respect to z (\mathbf{k} is the unit vector in the z -direction).

The flow regime in the lattice is defined by evaluating the Reynolds number Re as:

$$Re = \frac{\rho D_h v_e}{\mu} \quad (4)$$

where ρ is the fluid density, μ the viscosity and D_h is the hydraulic diameter, defined in Eq. (5):

$$D_h = 4 \frac{V_f}{A_w} \quad (5)$$

Note that the value of D_h in Eq. (5) is closely related to the reciprocal of the values of the parameter $\frac{A_w}{V_f}$ reported in Table 1.

The porous velocity v_e in Eq. (4) is defined in Eq. (6) and obtained from the superficial velocity v_s (i.e., the channel area-averaged velocity in the absence of the TPMS) and the porosity:

$$v_e = v_s / \varphi \quad (6)$$

2.2. Performance assessment on the reduced computational domain

2.2.1. Simulation setup

A sketch of the model of the reduced computational domain is shown in Fig. 5, which also illustrates the boundary conditions used for all simulations. Note that the fluid region is extruded both before and after the TPMS. The 40 mm downstream extrusion was confirmed to effectively mitigate the influence of the imposed outlet boundary condition on the flow and temperature fields within the TPMS, as well as to prevent backflow at the outlet section. The inlet mass flow rate (with a uniform velocity on the cross section) is set at 0.125 kg/s, i.e. one-tenth of the maximum flow rate available for the entire tile, with 10 bar imposed at the outlet. This pressure level also gives the most conservative condition on the saturation temperature at the wall, taken as monitor for the occurrence of boiling. A uniform heat flux is applied to the top of the tungsten surface, while the bottom of the lattice is adiabatic, as well as all the walls of the

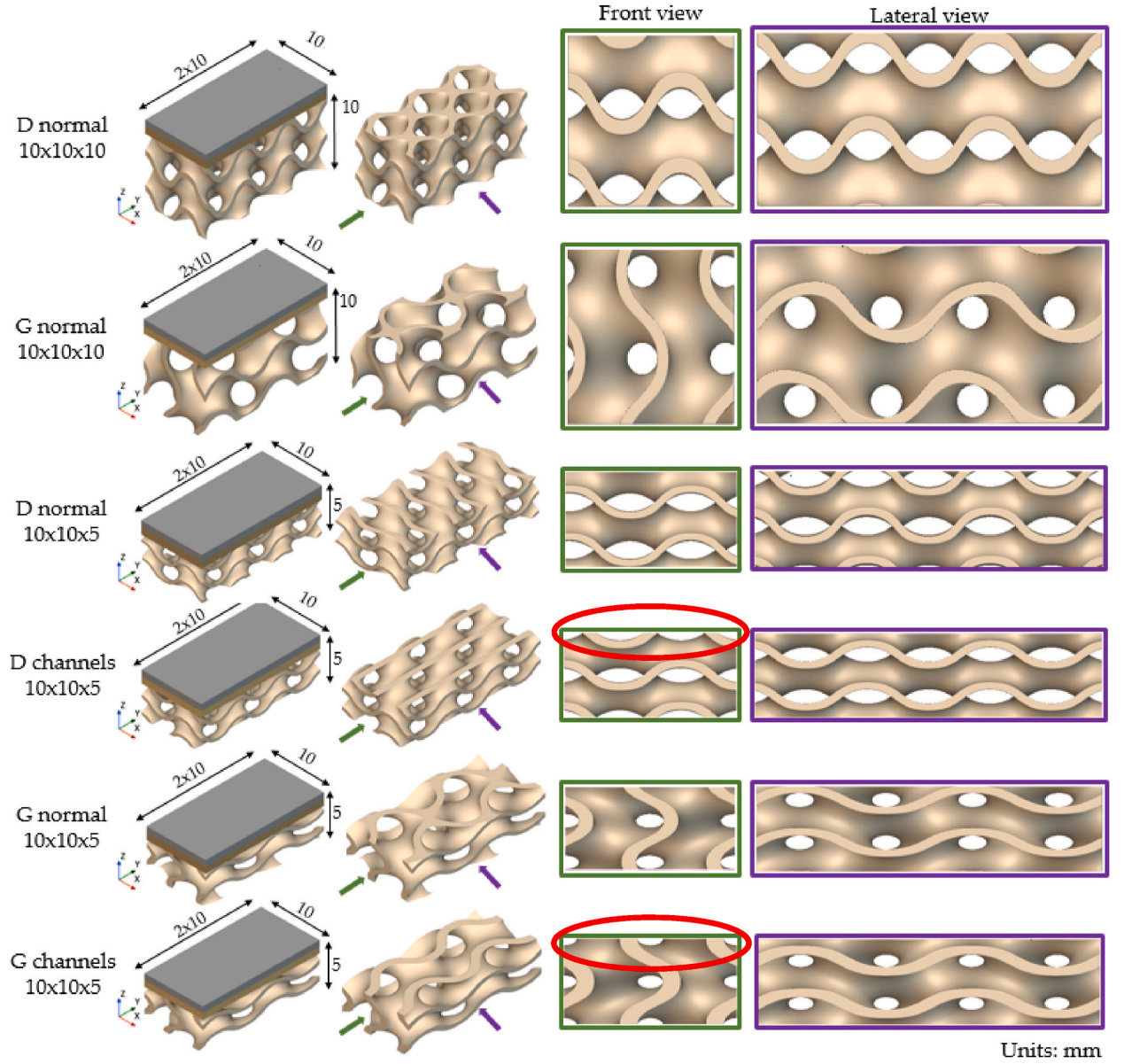


Fig. 4. – Lattice in the reduced computational domain adopted for a subset of the configurations reported in Table 1, and namely those with average wall thickness of the lattice set to 1 mm.

extruded sections. Periodic conditions are set on the two sides of the computational domain.

For the given mass flow rate, the computed values of the Re number, reported in Table 1, show that the flow is in turbulent regime for all selected configurations.

The commercial finite-volume software STAR-CCM+ was employed to numerically solve with finite volumes the steady-state Reynolds-averaged governing equations for the conjugate heat transfer problem. This includes the continuity equation (Eq. (7)), momentum equation (Eq. (8)), energy equation for the fluid phase (Eq. (9)), and energy equation for the solid phase (Eq. (10)).

$$\nabla \cdot \rho \vec{v} = 0 \quad (7)$$

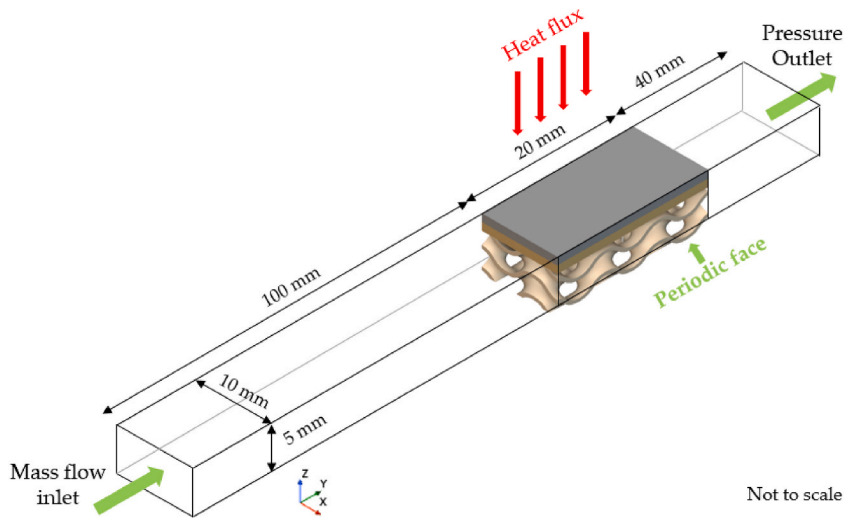
$$\rho \vec{v} \cdot \nabla \vec{v} = -\nabla p + \nabla \cdot ((\mu + \mu_t) \nabla \vec{v}) \quad (8)$$

$$\nabla \cdot (\rho \vec{v} h) = \nabla \cdot \left(\frac{\lambda + \lambda_t}{c_p} \nabla h \right) \quad (9)$$

Table 1

Geometrical parameters for the configurations analyzed in the reduced computational domain.

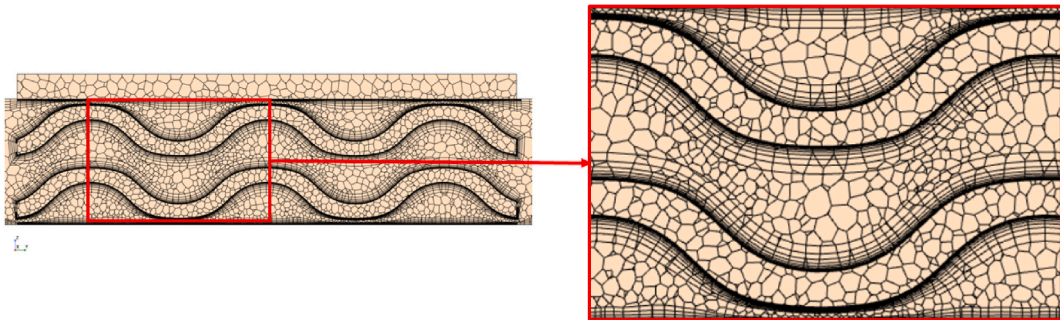
Topology	Unit cell width (mm)	Displacement	Wall thickness (mm)	ϕ (%)	$\frac{A_w}{V_f}$ [m ⁻¹]	Re
G	10	only N	0.8	81	0.8	11450
			1.0	76	0.9	11180
			1.2	72	1.0	10160
	5	N and C	0.8	80	0.9	11340
			1.0	76	1.0	11170
			1.2	71	1.1	10720
D	10	only N	0.8	81	1.3	8160
			1.0	76	1.4	8400
			1.2	71	1.5	8660
	5	N and C	0.8	77	1.4	8360
			1.0	71	1.5	8660
			1.2	65	1.6	9010

**Fig. 5.** Model setup for the simulations on the reduced computational domain, including the adopted boundary conditions.

$$\lambda_s \nabla^2 T = 0 \quad (10)$$

In Eqs. (7)–(10), μ_t is the turbulent viscosity, c_p is the specific heat and λ and λ_s are the fluid and solid thermal conductivities, respectively. The fluid pressure is p , whereas h the specific enthalpy and T the temperature.

The realizable $k - \varepsilon$ two-layer turbulence closure [22] was employed, as it has been suggested in Ref. [12] that it better reproduces hydraulic experimental data compared to the $k - \omega$ SST model. No boiling model is adopted, as the simulation target is to keep the fluid in single-phase.

**Fig. 6.** a) Diamond $10 \times 10 \times 5$ mm³ and the wall thickness of 1.2 mm wall thickness mesh in a plane along the direction of the flow in the center of the domain with a zoom in the central part.

The simulation adopts a segregated scheme and the SIMPLE algorithm for effective pressure-velocity coupling, with a second order scheme for the discretization of the pressure terms.

The thermodynamic properties of the coolant used here (subcooled water) are taken from IAPWS database. The properties of the CuCrZr and tungsten (thermal conductivity of 398 W/mK and 163.2 W/mK, respectively) are assumed constant with temperature. The mesh of **D** with lattice cell size $10 \times 10 \times 5 \text{ mm}^3$ and the wall thickness of 1.2 mm is shown in Fig. 6. The polyhedral mesh has ~ 0.7 Mcells, with 10 prism layers at the wall, targeting $y^+ \sim 1$ on the entire TPMS surface. The reduced computational domain has a mesh size, as well as a computational time, reduced by 1/60 with respect to the whole tile. The numerical uncertainty on the computed value of the maximum temperature increase on the heated surface and on the computed value of the pressure drop has been assessed by the GCI method [23] and it turned out to be $\pm 12^\circ\text{C}$ and $\pm 0.002 \text{ MPa}$, respectively. The numerical uncertainty on the solid surface at the interface with the coolant is only $\pm 1.3^\circ\text{C}$.

The simulations on the reduced computational domain were conducted by incrementally raising the heat flux until the saturation temperature was initially attained at the interface between water and CuCrZr. Furthermore, to better understand the heat removal properties of the different lattices, simulations with an imposed temperature on the heated surface were also performed, for a subset of lattice configurations (the ones in bold in Table 1).

2.2.2. Data reduction

The computed results are ranked in the performance space, defined by two key performance indicators (KPI), and namely the maximum heat flux that keeps the water-solid interface below the saturation temperature and by the pressure drop on the lattice. This ranking allows identifying the configurations reaching the target heat flux, but keeping at the same time the pressure drop in a range that, when the configuration is extended to the entire tile, guarantees to stay below 0.75 MPa. This constraint would allow the cooling circuit configuration in Fig. 1c.

The two KPIs have been then carefully investigated separately, to understand the influence and effect of the features of the different lattices on the computed KPI values.

Looking with more detail at the pressure drop Δp induced by the different lattices, an attempt to interpret it as a function of the geometrical features of the lattice has been made. The variable used for the correlation puts together the lattice length L , hydraulic diameter D_h and the tortuosity τ of the flow path, defined as in Eq. (11), in the dimensionless parameter $\tau \times D_h/L$. Note that this parameter allows comparing the behavior of lattices with the same topology but different pattern, e.g., the \mathbb{N} and \mathbb{C} configurations, where D_h is the same but τ is different, to that of different topologies, for which we know that the hydraulic diameter is different but we don't have a clear feeling about the tortuosity.

$$\tau = \frac{v_m}{v_y} \quad (11)$$

In Eq. (10), v_m is the volume average of the velocity magnitude in all the domain and v_y is volume-averaged of the velocity in the flow direction. To get a more straightforward interpretation of the results, this analysis has been performed on simulations where the lattice is kept isothermal, or where the heated surface is kept at a uniform temperature, rather than imposing a heat flux.

The maximum heat flux that a configuration can sustain has been correlated to the average heat transfer coefficient \overline{HTC} of the different lattices. The values of \overline{HTC} have been evaluated in a dedicated numerical study on a selection of configurations, imposing again a uniform surface temperature. The heat transferred to the coolant has been computed using Eq. (12):

$$\dot{m}c_p (T_{m,out} - T_{m,in}) = \overline{HTC} A_s \Delta T_{lm} \quad (12)$$

where A_s is the area of the heated surface and ΔT_{lm} in the mean logarithmic temperature, defined as a function of the surface tem-

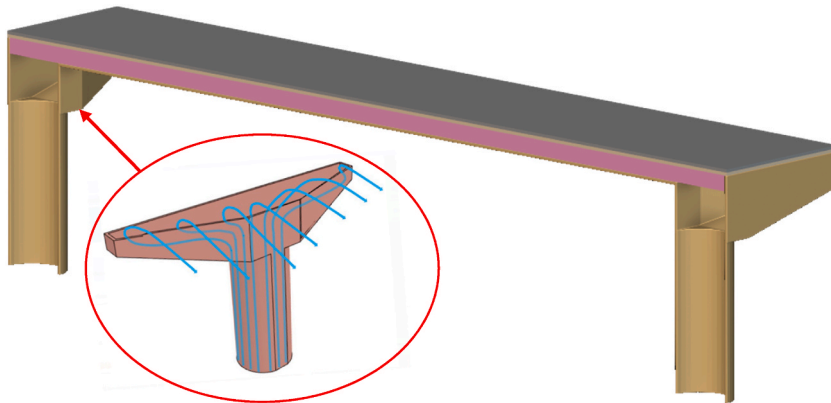


Fig. 7. Sketch of the entire tile, equipped with an inlet and an outlet duct. The cooling structure (in pink) is the best-performing TPMS lattice. The inset clarifies the shape of the inlet/outlet manifolds. (For interpretation of the references to color in this figure legend, the reader is referred to the Web version of this article.)

perature T_s and inlet and outlet mean temperatures $T_{m,i}$ and $T_{m,o}$ as

$$\Delta T_{lm} = \frac{(T_s - T_{m,o}) - (T_s - T_{m,i})}{\ln[(T_s - T_{m,o}) / (T_s - T_{m,i})]} \quad (13)$$

Having clarified the thermal-hydraulic performance of the different configurations, the selection of the most suited configuration to be adopted as cooling lattice for the entire tile was performed to guarantee the target heat flux at the minimum pressure drop.

2.3. Design and performance assessment of the divertor tile with the selected lattice

The analysis of the entire tile, configured with single inlet and outlet ducts having an inner diameter of 20 mm as shown in Fig. 7 and incorporating the most suitable TPMS lattice configuration, was carried out. The inlet and outlet manifolds were designed with a wedge shape in both longitudinal and transverse directions, to allow a more homogeneous flow distribution across the 10 mm width of the tile.

An inlet mass flow rate of 1.25 kg/s, corresponding to $\frac{1}{4}$ of the total mass flow rate in one whole divertor module (see Fig. 1c) and an outlet pressure of 10 bar were imposed. A uniform heat flux of 10 MW/m² was uniformly applied over a 10 cm length for three different heating scenarios: the initial 10 cm of the tile was heated (S1); the central 10 cm was heated (S2); the last 10 cm was heated (S3), to verify the compliance of the device with the constraints (no boiling, pressure drop below 0.75 MPa).

3. Results

3.1. Reduced computational domain analyses

The results in Fig. 8a show that the D lattice in the C configuration is capable to withstand up to 13 MW/m², a higher heat flux than

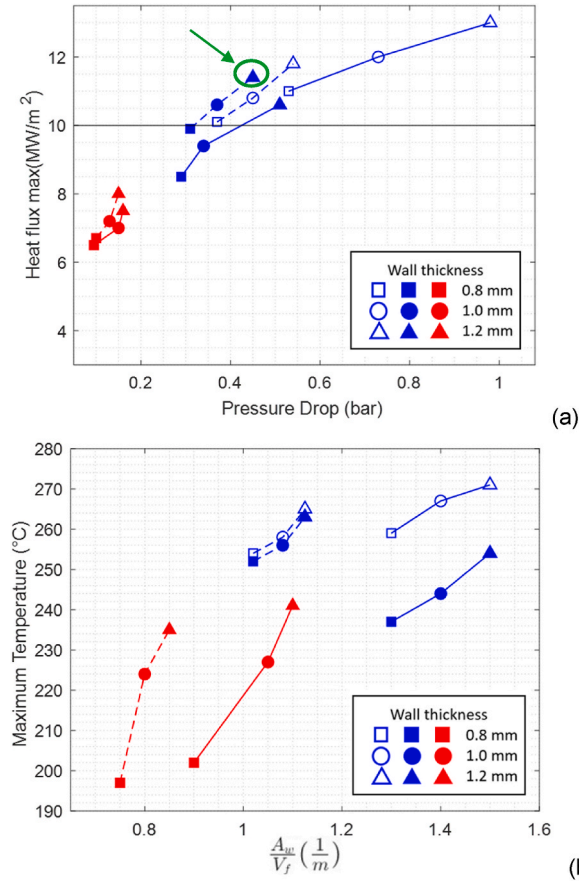


Fig. 8. (a) Maximum heat flux that the lattice in the reduced domain can sustain without overcoming the saturation temperature at the interface, plotted as a function the computed pressure drop. (b) Maximum surface temperature computed for the tungsten, as a function of the geometrical parameter A_w/V_f . Red symbols correspond to lattice unit cells of $10 \times 10 \times 10 \text{ mm}^3$, while blue symbols refer to $10 \times 10 \times 5 \text{ mm}^3$ in N (solid symbols) and C configurations (open symbols), respectively. Results for D lattices are connected with solid lines, results for G lattices are connected with dashed lines. (For interpretation of the references to color in this figure legend, the reader is referred to the Web version of this article.)

both the **G** lattices, but this is not true not in the **N** one, notwithstanding its higher surface-to-volume ratio, see Table 1. The much better performance of the **C** configuration if compared to the **N** one, which is true also for the **G** lattice although to a much lower extent, is qualitatively expected as the clear channels underneath the heated surface (see the ovals in Fig. 4) allow for a high convective heat transfer to the coolant. The displacement of the lattice with respect to the heated surface turns out to be of paramount relevance in determining the final performance: the **D** lattice in the **N** configuration is not able to efficiently exhaust the heat from the heated surface as the fluid is trapped in channels perpendicular to the main fluid direction, as visible in Fig. 2b. When the pressure loss in the structure is considered in the performance evaluation as in Fig. 8a, it becomes evident that the superior thermal performance of the **C** configurations comes at the cost of a much larger pressure drop across the reduce computational domain – in the case of the **D** lattice, the pressure drop is almost doubled in the **C** configuration, compared to the **N** one, while for the **G** lattice the increase in the pressure drop moving from **C** to **N** is about 20 %.

The maximum temperature computed on the heated surface when the maximum heat flux that still allows the coolant to remain in single phase is reported in Fig. 8b, clearly showing that all the considered structures keep the surface temperature well below 300 °C, even considering the estimated numerical accuracy of ± 12 °C. For all the considered lattices, the increase in the wall thickness pushes up the maximum bearable load and, as a consequence, the maximum tungsten temperature, in view of the decrease of the hydraulic diameter (increase in A_w/V_f in Fig. 8a) and the corresponding increase in the fluid velocity.

The dependence of the pressure drop on the displacement of each lattice with respect to the heated surface goes beyond any dependence on the porosity of the lattice, which is the same on the **N** and **C** configurations (see Table 1). The porosity is then not capable to explain the different hydraulic behaviors shown in Fig. 8a. In order to get a deeper insight on the effect of the lattice displacement on the pressure drop, this quantity is investigated in reduced computational domains with **D** and **G** lattices with ~ 71 % porosity in both **C** and **N** configurations (corresponding to the bold values in Table 1), for the given temperature values on the heated surface ($T_s = 26$ °C, 100 °C, 150 °C and 200 °C, respectively). The computed pressure drop for the 4 configurations, correlated to the dimensionless lattice geometrical parameter explained in Section 2.2, is shown in Fig. 9a. While the length of the lattice L is the same for all structures, the value of D_h can be correlated to the porosity as in Eq. (14):

$$D_h = 4 \frac{V_f}{V_{tot}} \frac{V_{tot}}{A_w} = \frac{4}{\phi} \frac{V_{tot}}{A_w} \quad (14)$$

Since A_w is the same for the **G** lattice in both **C** and **N** configurations, and for the **D** lattice in both configurations, the value of D_h clearly identify the lattice with a given porosity. The value of the tortuosity for the same lattice, as opposed to that, is affected by the displacement of the lattice. This can be explained looking again at the front views in Fig. 4: for the **C** configurations, the presence of the clear channel cross leads to a smaller tortuosity. With a larger average velocity in the direction of the flow, for the given D_h and L , the pressure drop of the **C** configurations is larger than that of the corresponding **N** configurations. The above-explained effects remain consistent at all temperature levels explored in the simulations. If the focus is shifted to the comparison between the behavior of **D** and **G** lattices in the similar configuration, the higher pressure drop computed in the **D** lattice is driven mainly by the larger surface-to-volume ratio, listed in Table 1, leading to a smaller hydraulic diameter.

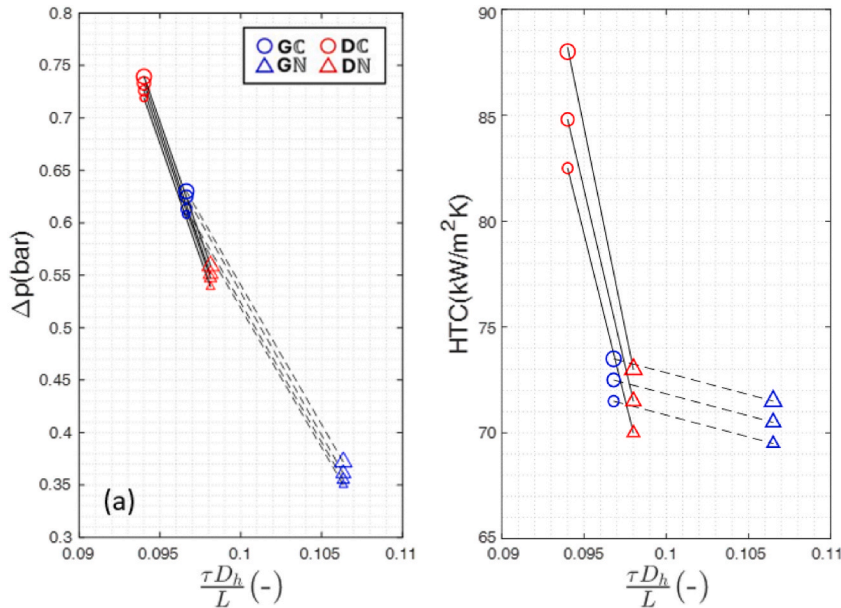


Fig. 9. (a) Pressure drop and (b) \overline{HTC} for the lattice configurations with porosity of 71 %, as a function of the geometrical parameter of the lattice. The size of the symbols is ranked by the temperature T_s imposed on the heated surface, from the smallest one (26 °C in (a) and 100 °C in (b)) to the largest one (200 °C).

Moving now to the explanation of the heat removal capability of the different lattices, Fig. 9b reports the values of the \overline{HTC} evaluated from Eqs. (12) and (13) for the different lattices, for different values of the surface temperature imposed in the simulations. Note that this comparison is useful to understand the main heat transfer features of the different structures, as in steady-state the lattice with the highest average outlet temperature will reveal immediately a best heat removal capability. It is shown that the configuration showing the highest values of \overline{HTC} is in all cases the **D C**, which is also the one capable to withstand the highest heat flux in Fig. 8b. In the comparison between the **N** and **C** configurations of the same lattice, the higher \overline{HTC} values computed for the **C** configurations can be explained as an effect of the larger longitudinal velocity, compared to the average value, affecting directly the heat removal from the heated surface in view of the presence of the clear channels immediately underneath the heated surface. This result somehow contradicts what is shown in Ref. [12], where the absence of clear channels was shown to result in a higher heat transfer, for a diamond lattice with no rotation with respect to the flow direction (see Section 2.1 and Fig. 2). Note, however, that the range of Re there was significantly lower than the values considered here, thus the effect of the convective heat transfer was possibly significantly reduced, compared to the contribution of conduction in the metal lattice.

The comparison between **D C** and **G C** shows that the \overline{HTC} of the former is 15%–20 % larger than the latter. This can be explained by geometrical considerations. Underneath the heated tungsten, the surface extension exposed to the fluid in the clear channels is much larger in the **D C** lattice, compared to the **G C** lattice, as visible by counting the number of the clear channels in Fig. 4a, pinpointed in the red ovals. Moreover, the **D C** lattice has a smaller tortuosity, i.e. a larger longitudinal component of the velocity, compared to the **G C**. The heat removal due to direct convective heat transfer to the coolant is thus much larger in the **D C** configuration than in the **G C** one. If the **N** configuration is considered, it gives for both structures a lower \overline{HTC} than the corresponding **C** configurations, as the heat transfer by convection to the coolant flowing underneath the heated surface fails because of the lack of any clear channels there. Note that there is a clear analogy between the picture of the pressure drop and that of the heat transfer coefficient. This confirms the results already shown in Ref. [11], where the Nusselt number was found to match very well the shear stress magnitude along a gyroid structure.

Regarding the selection of the optimal lattice for the entire divertor tile, it is important to note that the constraint on the global pressure drop for the tile drives the selection of structures with a pressure drop below 0.05 MPa ($0.75 \text{ MPa}/15 = 0.05 \text{ MPa}$). However, to account for numerical uncertainties in simulations ($\pm 0.002 \text{ MPa}$), and minor losses due to the inlet and outlet ducts, this threshold should be conservatively further reduced. A reasonable target are lattices with pressure drop values below 0.045 MPa. This constraint *de facto* rules out all lattices in the **C** configuration, despite their excellent thermal performance. Indeed, the **G C** configuration with the highest porosity would meet the requirement on the pressure drop, but meets only marginally the requirement of withstanding a minimum heat flux of 10 MW/m^2 . Based on the computed results and constraints, the selected lattice to be used for the analysis of the full tile is the **G** in **N** configuration, with lattice thickness of 1.2 mm and porosity of 71 %. This is the best structure, among those investigated, capable to withstand 10 MW/m^2 while maintaining a pressure drop below 0.045 MPa. The **G N** configuration with lattice thickness of 1 mm is more conservative form the point of view of the pressure drop, but can withstand a lower heat flux.

3.2. Divertor tile analysis

The simulation performed on the entire tile equipped with the **G** lattice with unit cell size of $10 \text{ mm} \times 10 \text{ mm} \times 5 \text{ mm}$ in **N** configuration confirms that the total pressure drop is 0.59 MPa when the coolant mass flow rate is 1.25 kg/s . Even accounting for a numerical uncertainty of $(15 \times \pm 0.002 \text{ MPa}) = \pm 0.03 \text{ MPa}$, the constraint of keeping the pressure drop of the entire tile below the value of 0.75 MPa is respected. When the heat flux of 10 MW/m^2 is applied to a length of 10 cm along the tile, the hot spot temperature remains below 275°C independently on the location of the applied heating, as shown in Fig. 10. In the case the heat flux is not at the inlet or outlet of the tile, the surface temperature remains below 250°C (Fig. 10b). The zig-zag bands with a lighter color, visible in all temperature maps of the heated surface of the tile in Fig. 10, are the marker of the fluid paths in the lattice. In all conditions reported in Fig. 10 the saturation temperature (evaluated at the outlet pressure) is not reached at the solid-coolant interface, so that the coolant remains in single phase, except for very limited locations at the inlet/outlet manifolds (Fig. 10a and c). The limited boiling occurring there (purple zones in Fig. 10a–c) is due to the entrance/exiting effects and to the manifold design, which is not optimized. This small spots where the fluid can undergo boiling could be avoided with a tailored shape of manifolds and ducts, or shifting to a more efficient lattice (**D C**, for instance, or hybrid structures as suggested in Ref. [24]) in the first and last, say, 10 mm of the tile. In all cases, the heated tungsten temperature remains well below the limit value, even when the numerical uncertainty on the computed temperature is considered.

Note, however, that the capability to withstand the expected heat flux in the entire region included between the inlet/outlet ducts (S2 case) totally confirms the suitability of the adopted design workflow, with the selection of the lattice based on the results of the reduced geometrical domain.

4. Discussion and perspectives

The performance of the tile cooling design proposed here is eventually compared with that already been proposed in Ref. [8], based on micro-channels (MC). For the same water mass flow rate, 1.25 kg/s , the best MC tile design in Ref. [8] could withstand a maximum heat flux of 8.8 MW/m^2 with a pressure drop of 0.94 MPa. The high value of pressure drop forces the adoption of the cooling solution with two coolant loops as in Fig. 1b, implying a higher investment cost for each divertor module. In the design proposed here, the tile could bear the nominal heat flux (with the exception of the inlet and outlet regions), and the reduced pressure drop, compared to the

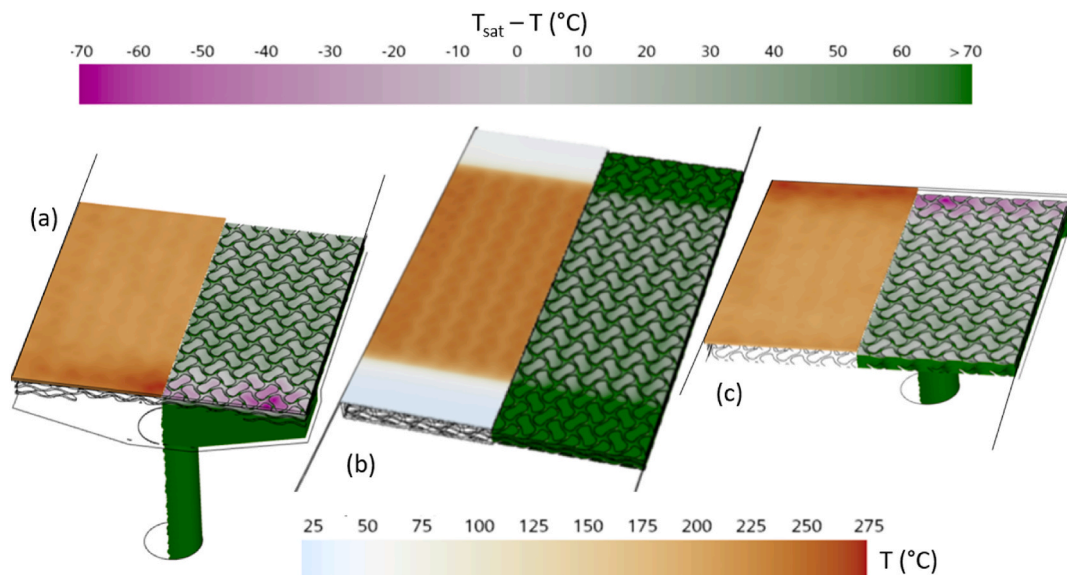


Fig. 10. Computed temperature maps for the tile equipped with TPMS, in the heating case S1 (a), S2 (b) and S3 (c). In each subplot, the temperature of the heated surface of the tungsten is shown on the left side of the tile, referring to the bottom temperature scale, while the map of the difference between the saturation temperature T_{sat} and the temperature of the interface between solid and fluid is shown on the fluid domain on the right part of the tile, with colors referred to the top temperature scale. (For interpretation of the references to color in this figure legend, the reader is referred to the Web version of this article.)

MC solution, allows for a single cooling loop per divertor module.

For the rated values of heat flux, the maximum estimated tungsten temperature in the MC design is 220 °C, and it stays below 250 °C in the TPMS design (S2 case). Note however that the latter value would be lower if the lower heat flux retained for the MC design is adopted, and a linear rescaling of the hot spot temperature would bring the TPMS design to a value similar to that of the MC design. As far as the cost of the tile itself is concerned, the Cu mass of the tile equipped with micro-channels is ~ 4.8 kg, while in the TPMS design it is just 1.75 kg, resulting in a significant material saving, lower costs and ease of remote maintenance. Both designs allows achieving much lower temperatures than those reported in Ref. [3], showing the expected beneficial effect of keeping the tungsten layer thickness at 1 mm.

As a general comment, it is now pretty clear that the AM of TPMS realized using the Laser-Powder Bed Fusion (L-PBF) technique for metals suffers from a significant surface roughness after de-powdering [25]. From the simulations on the tile equipped with the TPMS lattice, it is shown that there is still room to accommodate a 30 % increase in the pressure drop, but tests are needed to verify that the effect of the surface roughness could be kept under control (and below a 30 % increase on the pressure drop). However, note that, as an increase in the pressure drop is expected to be accompanied by an increase in the heat transfer coefficient, as discussed above, the same heat flux could be possibly withstood by a slightly lower mass flow rate, leading then to a reduction of the pressure drop. To clarify the effect of roughness and the credibility of RANS simulation when predicting the thermal-hydraulic performance of TPMS lattice manufactured both from metals and from resins, the authors are currently undergoing an extensive validation campaign based on the comparison of a wide variety of experimental results on TPMS samples manufactured in metals and resins to numerical results obtained using different turbulence closures.

The logical step to be performed at this stage would be the manufacturing of a tile mock-up, to confirm the printability, and a thermal-hydraulic test campaign in relevant conditions, to confirm the design performance. Moreover, a thermo-mechanical analysis is envisaged as it would help understanding the thermal stresses in the structure and the possible occurrence of delamination of the layered materials.

CRediT authorship contribution statement

Alessio Quamori Tanzi: Visualization, Validation, Software, Methodology, Investigation, Formal analysis, Data curation. **Antonio Cammi:** Writing – review & editing, Supervision, Methodology, Formal analysis, Conceptualization. **Luca Marocco:** Writing – review & editing, Supervision, Methodology, Investigation, Formal analysis, Conceptualization. **Laura Savoldi:** Writing – original draft, Visualization, Resources, Project administration, Methodology, Investigation, Formal analysis, Conceptualization.

Declaration of competing interest

The authors declare that they have no known competing financial interests or personal relationships that could have appeared to

influence the work reported in this paper.

Acknowledgements

This work has been carried out within the framework of the EUROfusion Consortium, partly funded by the European Union via the Euratom Research and Training Programme (Grant Agreement No 101052200 — EUROfusion). Views and opinions expressed are however those of the author(s) only and do not necessarily reflect those of the European Union or the European Commission. Neither the European Union nor the European Commission can be held responsible for them. Views and opinions expressed are those of the authors only and do not necessarily reflect those of the European Union or the European Commission. Neither the European Union nor the European Commission can be held responsible for them. The work of A.Q.T. is partially funded by Eni S. p.A.

Data availability

Data will be made available on request.

References

- [1] R. Albanese, A. Pizzuto, The DTT proposal. A tokamak facility to address exhaust challenges for DEMO: introduction and executive summary, *Fusion Eng. Des.* 122 (nov. 2017) 274–284, <https://doi.org/10.1016/j.fusengdes.2016.12.030>.
- [2] V. Bykov, et al., Structural analysis of W7-X: from design to assembly and operation, *Fusion Eng. Des.* 86 (6–8) (ott. 2011) 645–650, <https://doi.org/10.1016/j.fusengdes.2011.01.019>, fasc.
- [3] J. Boscary, et al., Conceptual design of the next generation of W7-X divertor W-target elements, *Fusion Eng. Des.* 192 (2023) 113629, <https://doi.org/10.1016/j.fusengdes.2023.113629> lug.
- [4] The divertor», [Online]. Disponibile su: <https://www.iter.org/mach/Divertor>.
- [5] J.H. You, et al., Divertor of the European DEMO: engineering and technologies for power exhaust, *Fusion Eng. Des.* 175 (feb. 2022) 113010, <https://doi.org/10.1016/j.fusengdes.2022.113010>.
- [6] H. Ebadi, et al., A multi-scale hybrid approach to the modelling and design of a novel micro-channel cooling structure for the W7X divertor, *Case Stud. Therm. Eng.* 42 (feb. 2023) 102734, <https://doi.org/10.1016/j.csite.2023.102734>.
- [7] J. Fellingner, et al., Tungsten based divertor development for Wendelstein 7-X, *Nucl. Mater. Energy* 37 (2023) 101506, <https://doi.org/10.1016/j.nme.2023.101506> dic.
- [8] F. Carrone, R. Difonzo, J. Fellingner, L. Savoldi, Multi-scale lumped modeling of micro-channels cooling structure for W7-X divertor unit target module, *Fusion Eng. Des.* 204 (2024) 114481, <https://doi.org/10.1016/j.fusengdes.2024.114481> lug.
- [9] E. Gajetti, G. Boccardo, A. Buffo, L. Marocco, C. Piatti, L. Savoldi, Assessment of the use of triply periodic minimal surfaces as heat SINKS for MW/M²-HEAT flux class components, in: *Proceeding of International Heat Transfer Conference 17*, Cape Town, South Africa: Begellhouse, 2023, p. 10, <https://doi.org/10.1615/IHTC17.210-370>.
- [10] E. Gajetti, et al., A new efficient mirror cooling for the transmission line of fusion reactor ECH systems based on triply periodic minimal surfaces, *IEEE Trans. Plasma Sci.* (2024) 1–7, <https://doi.org/10.1109/TPS.2024.3383275>.
- [11] W. Li, G. Yu, Z. Yu, Bioinspired heat exchangers based on triply periodic minimal surfaces for supercritical CO₂ cycles, *Appl. Therm. Eng.* 179 (2020), <https://doi.org/10.1016/j.applthermaleng.2020.115686>.
- [12] W. Tang, et al., Analysis on the convective heat transfer process and performance evaluation of triply periodic minimal surface (TPMS) based on diamond, gyroid and iwp, *Int. J. Heat Mass Transf.* 201 (feb. 2023) 123642, <https://doi.org/10.1016/j.ijheatmasstransfer.2022.123642>.
- [13] Z. Cheng, R. Xu, P.-X. Jiang, Morphology, flow and heat transfer in triply periodic minimal surface based porous structures, *Int. J. Heat Mass Transf.* 170 (2021), <https://doi.org/10.1016/j.ijheatmasstransfer.2021.120902>.
- [14] J. Iyer, T. Moore, D. Nguyen, P. Roy, J. Stolaroff, Heat transfer and pressure drop characteristics of heat exchangers based on triply periodic minimal and periodic nodal surfaces, *Appl. Therm. Eng.* 209 (2022), <https://doi.org/10.1016/j.applthermaleng.2022.118192>.
- [15] Z. Cheng, X. Li, R. Xu, P. Jiang, Investigations on porous media customized by triply periodic minimal surface: heat transfer correlations and strength performance, *Int. Commun. Heat Mass Transf.* 129 (2021) [Online]. Disponibile su: www.scopus.com.
- [16] Next-Generation Engineering Design Software | NTopology [Online]. Available at: <https://ntopology.com/>.
- [17] A. Mortazavi, et al., Experimental investigation of triply periodic minimal surfaces for high-temperature solar receivers, *Case Stud. Therm. Eng.* 60 (2024) 104771, <https://doi.org/10.1016/j.csite.2024.104771> ago.
- [18] O. Ibhade, The effects of cell stretching on the thermal and flow characteristics of triply periodic minimal surfaces, *Int. Commun. Heat Mass Transf.* 153 (apr. 2024) 107364, <https://doi.org/10.1016/j.icheatmasstransfer.2024.107364>.
- [19] A. Pepato, INFN Padua, Private Communication, 2024.
- [20] R. Attarzadeh, S.-H. Attarzadeh-Niaki, C. Duwig, Multi-objective optimization of TPMS-based heat exchangers for low-temperature waste heat recovery, *Appl. Therm. Eng.* 212 (2022), <https://doi.org/10.1016/j.applthermaleng.2022.118448>.
- [21] R. Attarzadeh, M. Rovira, C. Duwig, Design analysis of the "Schwartz D" based heat exchanger: a numerical study, *Int. J. Heat Mass Transf.* 177 (2021), <https://doi.org/10.1016/j.ijheatmasstransfer.2021.121415>.
- [22] Simcenter STAR-CCM+ [Online]. Available at: <https://www.plm.automation.siemens.com/global/it/products/simcenter/STAR-CCM.html>.
- [23] Standard for Verification and Validation in Computational Fluid Dynamics and Heat Transfer. [Online]. Available at: <https://www.asme.org/codes-standards/find-codes-standards/standard-for-verification-and-validation-in-computational-fluid-dynamics-and-heat-transfer>.
- [24] H. Xu, W. Yu, Y. Zhang, S. Ma, Z. Wu, X. Liu, Flow and heat transfer performance of bionic heat transfer structures with hybrid triply periodic minimal surfaces, *Appl. Energy* 351 (2023) 121847, <https://doi.org/10.1016/j.apenergy.2023.121847> dic.
- [25] M.B. Hawken, S. Reid, D.A. Clarke, M. Watson, C.J. Fee, D.J. Holland, Characterization of pressure drop through Schwarz-Diamond triply periodic minimal surface porous media, *Chem. Eng. Sci.* 280 (2023) 119039.